DOI: 10.1002/ ((please add manuscript number))
Article type: Full Paper

Title: Investigation of Nano-Sized Cu(II)O As a High Capacity Conversion Material for Li Metal Cells and Lithium Ion Full Cells

*Yunxian Qian, Philip Niehoff, Dong Zhou, Robert Adam, Daria Mikhailova, Marcelina Pyschik, Markus Börner, Richard Klöpsch, David Rafaja, Gerhard Schumacher, Helmut Ehrenberg, Martin Winter, and Falko Schappacher**

Y.X.Qian, Dr. P. Niehoff, M. Pyschik, M. Börner, Dr. R. Klöpsch, Prof. M. Winter, Dr. F. Schappacher
MEET Battery Research Center, Institute of Physical Chemistry, Westfaelische Wilhelms-Universitaet Muenster, Corrensstr. 46, 48161, Muenster, Germany
E-mail: *falko.schappacher@uni-muenster.de*
D. Zhou, Prof. G. Schumacher
Helmholtz-Zentrum Berlin für Materialien und Energie, Hahn-Meitner-Platz 1, 14109 Berlin, Germany
R. Adam, Prof. D. Rafaja
TU Bergakademie Freiberg, Institute of Materials Science, Gustav-Zeuner-Str. 5, 09599 Freiberg, Germany
Dr. D. Mikhailova, Prof. H. Ehrenberg
Karlsruhe Institute of Technology (KIT), Institute of Applied Materials (IAM), Hermann-von-Helmholtz-Platz 1, D-76344 Eggenstein-Leopoldshafen, Germany
Prof. M. Winter
Helmholtz Institute Muenster, IEK-12, Forschungszentrum Jülich GmbH, Corrensstr. 46, 48149 Muenster, Germany

Keywords: Solid electrolyte interphase (SEI), nanostructured CuO electrode, conversion reaction mechanism, lithium ion batteries, NMC 111/CuO full cell

In this study, nanostructured CuO electrodes are prepared, which show no capacity decay for 40 cycles at 0.1C for Li metal cell setup. The reaction mechanisms of the CuO electrodes are investigated as the main focus. With the help of *in situ* EIS, *in situ* XRD, TEM, XAS, SQUID, IC and GC-MS, it is found that the as-prepared CuO electrode undergoes significant phase and composition changes during the initial lithiation, with the transformation of CuO to nano-crystalline Cu. During the 1st delithiation, Cu is inhomogeneously oxidized, which yields a mixture of Cu_2O, $Cu_{2-x}O$ and Cu. The incomplete conversion reaction during the 1st cycle is attended by the formation and partial decomposition of the SEI as the side reactions.

Nevertheless, from the 1st to 5th delithiation, the oxidation state of Cu approaches +2. After an additional formation step, the transformation to Cu and back to $Cu_{2-x}O$ keeps stable during the subsequent long-term cycling with no electrolyte decomposition products detected. The NMC/CuO full cells show high capacities (655.8 ± 0.6, 618.6 ± 0.9 and 290 ± 2 mAh/g at 0.1, 1 and 10C, respectively), within the voltage range of 0.7-4.0V at 20°C and a high capacity retention (85% after 200 cycles at 1C).

1. Introduction

CuO has been used as cathode material in CuO/Li metal primary battery cells for more than 30 years. The discharge reaction mechanism has been investigated ever since.[1] However, debates still exist regarding whether composites containing intermediate phases are formed during the electrochemical discharge.[2-4] As other materials that have been first proposed as cathodes in Li metal batteries,[5,6] CuO has become a candidate for the anode of lithium-ion battery cells because of its high theoretical capacity, nontoxic nature and the reversible conversion reaction with Li (found by Poizot *et al.* in 2000).[7,8] Due to their limited specific capacities (Ah/kg), the traditional anode material for lithium-ion batteries, i.e., graphitic carbon such as synthetic mesocarbon microbead (MCMB) graphite or natural graphite is under challenge by materials like CuO as a conversion reaction based material.[9,10] Nevertheless, because of the high discharge potential, most graphite anode based lithium cells show larger specific energies (Wh/kg), though conversion anodes may have an advantage in volumetric capacities (Ah/L) and related energy densities (Wh/L). At the end, unfortunately, the large potential hysteresis [11] results in poor voltage efficiency and also the lower Coulombic efficiency (in particular in the first cycle). These disadvantages significantly lower energy efficiencies of conversion anodes and thus cause higher electricity losses and higher charging costs.[12] Hence, the application of conversion materials might be restricted to certain areas in which energy efficiency is not the primary concern, e.g. for small cell size applications, such as portable consumer electronics.

As a typical conversion material, CuO experiences huge volume changes (more than 70 %) during the initial lithiation process.[13] It has been reported that this volume change might be the main reason for the rapid capacity loss (more than 70 %) during the initial cycles.[14] The low capacity is caused by a re-oxidation of copper to Cu_2O only that has an oxidation state of Cu +1.[15] The theoretical capacity related to this re-oxidation is 375 mAh/g. It was found that in re-oxidized copper oxides the small crystallite size facilitates formation of cubic Cu_2O instead of monoclinic CuO.[16] Based on the previous experience made with Li storage metal (Sn, Si, etc.) morphologies,[17] many research groups have adopted various synthesis methods to minimize the side effects resulting from volume expansion of conversion materials. For example, Tang et al. synthesized a leaf-like mesoporous CuO with a high current density and a specific capacity of 490.5 mAh/g.[7] Moreover, CuO nanotubes, thin film and other porous morphologies as well as surface-organic coating and CuO/graphite composites were prepared to enhance the Coulombic efficiency and cycling performance.[18-20] However, the Coulombic efficiency of these methods remains questionable as regarding to their impact on the long-term electrochemical performance. Moreover, the nature of the conversion mechanism between Li and CuO still remains ambiguous. Finally, few reports have been published, which address the full-cell performance by assembling CuO anodes with commercially available cathodes to investigate the real electrochemical conditions of this kind of lithium-ion batteries.

In this work, nanostructured CuO electrodes are prepared with commercially available raw materials. CuO/Li metal cells are assembled and investigated. The mean voltage and the cell impedance are determined to figure out the impact of Li^+ diffusion and the solid electrolyte interphase (SEI) on the electrochemical properties of the Li metal cells.[21] Moreover, the main focus of this study is the investigation of the conversion reaction of CuO with Li during the initial lithiation/delithiation, where the highest degree of volume expansion and phase transformations take place. The combination of *in situ* X-ray diffraction (XRD), selected area

electron diffraction (SAED), energy dispersive X-ray spectroscopy (EDS), X-ray absorption spectroscopy (XAS) and superconducting quantum interference device (SQUID) measurements reveal the phase and oxidation state changes of the Cu-O-Li system at different voltage ranges. Besides, the corresponding transmission electron microscopy (TEM) images at the initial lithiation/delithiation states give an impression of the crystallite size and the thickness changes of the SEI,[22] which covers the active material and has been suggested to contribute to the capacity of the cell as well.[23] Furthermore, a lithium-ion battery full cell is assembled with the nanostructured CuO as anode and a commercial $LiNi_{1/3}Mn_{1/3}Co_{1/3}O_2$ (NMC-111) electrode as cathode for the demonstration of application under realistic conditions. The as-prepared full cell is investigated under different voltage ranges and C-rates to show its electrochemical properties. Meanwhile, the electrolyte decomposition is investigated with the help of ion chromatography (IC) and gas chromatography-mass spectrometry (GC-MS).

2. Results

The morphology of the pristine nano-sized CuO particles and the surface of the self-prepared electrodes were examined by SEM (Figure S1) and XRD (Figure S2). In the pristine state, CuO nano particles with an average diameter of ~ 50 nm are observed (Figure S1a). After the high speed ball milling, the self-casted electrodes retain the original grain size distribution of the raw particles, which are homogenously embedded in the conducting and binding auxiliary materials (Figure S1b). Rietveld refinement of the X-ray diffraction pattern from the casted electrode reveals phase-pure CuO (space group *C*2/*c*) with a crystallite size of 31 ± 2 nm and with the following set of unit cell parameters: a = 0.4684 ± 0.0003 nm, b = 0.3426 ± 0.0003 nm, c = 0.5132 ± 0.0004 nm, β = 99.42 ± 0.01 °.

To study the electrochemical properties of the nanostructured CuO electrodes, CuO/Li metal cells are assembled and undergo 40 constant current (CC) cycles at 0.1C, as shown in Figure 1.

The initial discharge (lithiation) capacity is 766 ± 1 mAh/g, while the first charge (delithiation) capacity is 381 ± 1 mAh/g. The Coulombic efficiency of the 1st cycle is 43 %. The low Coulombic efficiency of the 1st cycle is characteristic for this kind of active material.[24-27] It is commonly considered to be caused by the volume change and the formation of a solid electrolyte interphase (SEI) during the 1st cycle and the reoxidation of metallic Cu to Cu^{+1} in Cu_2O instead of to Cu^{+2} in CuO. However, the nano CuO/Li metal cells experience a continuous increase of the specific capacity upon cycling. After 40 cycles, the specific delithiation capacity increases from 381 ± 1 mAh/g to 550 ± 1 mAh/g, with the corresponding capacity increase of 44 %.

To investigate possible reasons behind this capacity increase during cycling, the data of the mean voltages of the nano CuO/Li metal cells are plotted in Figure 1 for the first 40 cycles. All data are extracted in the fully lithiated state. During cycling, a much lower lithiation mean voltage is seen during the initial cycles. Nevertheless, with the proceeding of cycling, the mean voltage value increases from 1.03 ± 0.01 to 1.14 ± 0.01 V. As an increase in the lithiation mean voltage indicates a decrease of the internal resistance, it can be seen that the internal resistance of the cell is decreased upon cycling, which results in the corresponding capacity increase for the investigated cells.

An electrochemical impedance spectroscopy (EIS) measurement was conducted to detect the charge-transfer and contact resistance of the cells during cycling, which indicate the changes in the corresponding SEI and the contact resistance of the electrode, as shown in Figure 2. The frequencies at 5–100 Hz reveal processes affected by the charge-transfer resistance, and frequencies of >100 Hz correspond to the contact resistances.[28] The constant charge-transfer resistance indicates the formation of an effective SEI after the 1st de-lithiation process, while the constant contact resistances show the stability of the corresponding electrodes during cycling.

Hence, combining the mean voltage analysis results with the EIS results, it is clear that the increase in the mean voltage (the decrease of the resistance) does not originate from the SEI, but is caused by a better Li^+ transport in the electrode.

In this regard, an additional constant voltage (CV) step at 0.02 and 3 V for 10h is applied in the first five formation cycles to take an advantage of the improved Li^+ diffusion on the electrochemical performance of the corresponding CuO/Li metal cells, as shown in Figure 3. It has been previously reported that an additional CV step during the charge and discharge have a most pronounced effect on the significance of the obtained CC cycling data.[29] Differences can clearly be seen from the delithiation capacities after the CV step compared with the cells without any further CV step. After the formation process, the charge (delithiation) capacity increases from 542 ± 5 (without a CV step) to 693 ± 2 mAh/g (with a CV step). After that, the cell keeps an average delithiated capacity of ≈ 580 mAh/g until the end of the 40th cycle.

Therefore, it can be concluded that the additional constant voltage step during the formation process enhances the capacity of the cell system.

The lithiation/delithiation voltage profiles of the nano CuO/Li cells are presented in Figure 4. During the initial and the following lithiation processes, three voltage regions at 2.1-1.4 V, 1.4-1.0 V and 1.0-0.02 V are seen, respectively. However, when comparing the 1st with the 5th and with the 40th lithiation profile, the region of 1.4-1.0V is shortened, while the other two voltage regions keep the same during cycling. Moreover, during the following 1st delithiation process, only two voltage regions are observed (at 0.02 - 2.25 V and 2.25 – 3.0 V). Meanwhile, a prolonged voltage region of 2.25 – 3.0 V is seen after the 5th delithiation when compared with the 1st delithiation. This indicates the proceeding of the conversion reaction, in which the mean oxidation state shifts toward +2. This assessment is further confirmed by the analysis of the Coulombic efficiency.

In the first lithiation/delithiation process, the Coulombic efficiency is only 62 %, as the specific capacities for the 1st lithiation and delithiation are 880 ± 5 and 546 ± 2 mAh/g, respectively). During the first lithiation/delithiation cycle, large changes in the phase composition occur, which are further investigated by XAS, XRD, SQUID and TEM measurements. In the 2nd cycle, the Coulombic efficiency increases to 106 % and stays above 100% during the following 40 cycles. This might be due to the fact that parts of charge invested in the first cycle (visible by the low Coulombic efficiency) can be re-gained in the following cycle, meaning that the amount of the re-oxidized Cu exceeds the previous reduction of the copper oxides, which is due to the existence of many metallic Cu residues after the initial delithiation. Nevertheless, the Coulombic efficiency becomes stable after the formation cycles, with a constant lithiation capacity of ≈ 580 mAh/g during the whole 40 CC cycles at 0.1C. Hence, it is of importance to figure out the reaction mechanism and the oxidation state of copper during the initial cycles.

Figure 5 presents the *in situ* XRD patterns collected during cycling together with the lithiation/delithiation voltage profiles. The four selected lithiation/delithiation periods in Figure 5a, labeled as I (start of the 1st lithiation), II (end of the 1st lithiation), III (end of the 1st delithiation) and IV (end of the 2nd lithiation) correspond to the four XRD patterns shown in Figure 5b. For pattern I, sharp CuO peaks are observed based on the high crystallinity of the nano-sized CuO powder. These characteristic peaks of CuO quickly fade away during the initial lithiation. As seen in pattern II, the intensity of the CuO peaks become weak, a broad Cu (111) line (space group $Fm\bar{3}m$) appears, representing the formation of metallic Cu by the conversion reaction. The broadening of the Cu peak is caused by the nano-crystalline nature of metallic Cu particles. The weak CuO content may origin from the isolated and unreacted particles in the electrode. Nevertheless, when it comes to the first delithiation process (pattern III), line broadening of peaks leads to indistinctness of the XRD pattern, which is caused by the low crystallinity of the active material, while the scattered electrons from SAED pattern (see Figure

6) with their shorter extinction length are more predestined to scatter coherently on much smaller crystallites then the X-rays. The XRD pattern after the 2nd lithiation (pattern IV) shows similar characteristic peaks to pattern II, with the presence of a broad Cu (111) peak and again the weak CuO peaks from isolated non-reacted particles. The characteristic Li_2O (111) peaks (space group $Fm\bar{3}m$) are both detected in the lithiated state (pattern II and IV). However, no Cu_2O phase (space group $Pn\bar{3}m$), which is an intermediate component for the conversion of CuO to Cu and the endmember for the delithiation reaction of metallic Cu,[15,30] is detected during the whole process. This as well might be caused by the low crystallinity and the long-range disordered structure of the formed products.

The presence of crystalline phases identified by XRD was verified by selected area electron diffraction (SAED) and energy dispersive X-ray spectroscopy (EDS). The EDS was mainly used to find the grains of active material containing Cu and its oxides. The SAED patterns shown in Figure 6 correspond to the *in situ* XRD patterns labeled as stages II and III in Figure 5. After the initial lithiation (Figures 6a and 6b), Cu and Li_2O are found in the SAED pattern. After the first delithiation (Figures 6c and 6d), the sample contained cubic Cu and Cu_2O according to SAED. However, no presence of crystalline monoclinic CuO phase was observed, even though several particles were investigated. This finding contradicts apparently the result of the CC/CV cycling (cf. Figure 4), which indicates a shift of the mean oxidation state toward +2. A possible explanation of this discrepancy is the formation of copper vacancies in the crystal structure of $Cu_{2-x}O$ that was observed during the low temperature oxidation of Cu thin films.[31,32] The formation of vacancies in $Cu_{2-x}O$ would rise the effective oxidation state in the delithiated sample beyond +1, but SAED could not distinguish $Cu_{2-x}O$ from Cu_2O with fully occupied Cu sublattice, because this method is not sufficiently sensitive to the occupancies of individual atomic positions. Also the change of the lattice parameter is too small to be recognized by electron diffraction in TEM.

As neither XRD nor SAED can give a reliable information about the oxidation state, the samples were analyzed additionally by XAS. The normalized Cu K-edge XAS spectra of the CuO anodes at various states of lithiation and the reference spectra of Cu, Cu_2O and CuO are shown in Figure 7. Since XAS spectra are very sensitive to the electronic structure of the absorbing atom, the average valence state of the absorbing atom is determined empirically by comparing shapes and energy of absorption edge features.[33] In Figure 7, as the cell is firstly lithiated down to 0.02 V, the corresponding spectrum is nearly identical to that of the pure Cu reference. This implies that CuO is transformed to Cu at the end of the 1st lithiation. During the following delithiation to 3.0 V, the main edge, which corresponds to the dipole-allowed 1s → 4p transition, shifts to ~ 8995 eV along with a shoulder at ~ 8980 eV. It appears at the energy position between that of the reference Cu_2O and CuO compounds. This shoulder is due to the presence of Cu, intermediate Cu_2O phases and a weak contribution of CuO phase as the cell is first delithiated to 3.0 V, while at 2.25 V, only the characteristic edge of Cu is found. Further, after 5 CC/CV cycles, the main edges of the lithiated samples (3.0 V) shift to ~ 8997 eV, which is nearly the same as that of the reference CuO (with an oxidations state of Cu with +2). However, a small bump at ~ 8981 eV is still observed. Both features indicate that with the proceeding of cycling the conversion reactions are more facilitated; more and more Cu is oxidized towards a mean oxidation state higher than +1 during the delithation process, while some Cu and Cu_2O still remain, even in the delithiated state.

In order to support the results of XAS regarding the oxidation state of copper, SQUID measurements were carried out that give information about the magnetic state of the copper oxides. Using SQUID, the temperature dependences of the magnetization (Figure 8) were measured both in the zero-field-cooled (ZFC) and in the field-cooled (FC) mode. No differences between these two modes were detected for the applied field strengths. Below 15 K, temperature-dependent measurements demonstrate a rise in magnetization, while field

dependence of magnetization shows a non-linear behavior up to room temperature, see inset in Figure 8.

The paramagnetic component in the material was calculated from the Curie-Weiss law $\chi = C/(T-\theta) + \chi_0$ applied to the molar magnetic susceptibility, which was normalized on a hypothetical formula unit [CuO], at 6 T in the temperature range between 50 and 300 K. The obtained parameters are C = 0.0612(4) emu*K/mol*Oe, θ = -18.8(4) K and $\chi_0 = 3.79(1)*10^{-4}$ emu/mol*Oe. The negative Weiss constant of -18.8(4) K indicates antiferromagnetic interactions in the material, although a non-linear development of the magnetization curve vs. magnetic field indicates also a ferromagnetic component. The Curie constant $C = N_A\mu_{eff}^2/3k_B$ was re-calculated into the paramagnetic effective moment μ_{eff} = 0.70(2) μ_B/f.u. with N_A being the Avogadro constant and k_B the Boltzmann constant.

Significant paramagnetic moment (μ_{eff} = 0.70(2) μ_B/f.u.) supports the hypothesis about the presence of Cu^{2+} ions in the aged CuO electrode. Assuming a paramagnetic moment of Cu^{2+} (d^9) of 1.73 μ_B/f.u. usually measured in oxides, the fraction of Cu^{2+} in the electrochemically reduced and subsequently oxidized $Cu_{2-x}O$ material of about 16 mol.% is estimated. Two possible scenarios can describe the existence of Cu^{2+} in $Cu_{2-x}O$: *i*) formation of cation vacancies with simultaneous oxidation of copper cations in the crystalline cubic $Cu_{2-x}O$, and *ii*) formation of amorphous CuO nano-layers on the surface of crystalline Cu_2O cores. According to the literature data, both nano-sized oxides $Cu_{2-x}O$ with cation vacancies[34] and amorphous CuO[35] can show a ferromagnetic component in the magnetization up to 300 K. However, since our field dependences of magnetization do not demonstrate any hysteresis loop like a nano-sized CuO,[35] we argue for accommodation of Cu^{2+} in the material rather in form of vacancies-containing cubic $Cu_{2-x}O$.

Combining the XAS and SQUID results, one can see that CuO is reduced to metallic Cu during the 1st lithiation process. Nevertheless, with the following delithiation to 3.0 V, a mixture of Cu, Cu_2O and $Cu_{2-x}O$ ($x < 1$) is formed. According to the results of SAED, $Cu_{2-x}O$ still has the crystal structure of cubic Cu_2O. Upon further cycling, the reactions between Cu, copper oxides and Li_2O are more facilitated, the average oxidation state of the delithiated copper oxides is shifted towards +2, with the retention of small amounts of Cu and cubic $Cu_{2-x}O$ in the delithiated samples. The incomplete conversion reaction for the 1st cycle with a left of metallic Cu in the delithiated state might be related to the electrolyte decomposition, and by the formation and decomposition of the SEI. These phenomena were investigated using other methods (SEM and TEM) in more details.

According to the scanning electron micrographs taken on the electrodes after the initial lithiation (Figure 9a), an SEI layer is likely to form, while after the following delithiation (Figure 9b), the particles get smaller as compared with the lithiated state. More elongated particles like rods, instead of spherical particles are seen. The change of the morphology is due to the multiple phase formation and decomposition processes.

The TEM and high resolution transmission electron micrographs (HRTEM) revealed that the thickness of the SEI is different in lithiated and delithiated state (Figure 10). The SEI of the lithiated particle (Figs. 10 a, b) is thicker in comparison to the SEI on the de-lithiated particle (Figs. 10 c, d). The HRTEM (Figs. 10 b, d) provides a closer insight into the amorphous SEI, and reveals the thickness of the de-lithiated particle of ≈5 nm and an average diameter value for the firstly lithiated particle of ≈10 nm.

Considering the high observed delithiation capacity (≈ 600 mAh/g) of the prepared electrodes, it can be concluded that the additional capacity comes from the partial oxidation of Cu_2O to

$Cu_{2-x}O$ ($x < 1$), from the electrolyte decomposition and the SEI formation and decomposition during the 1st cycle.

Based on the promising electrochemical properties of the CuO electrodes in Li metal cells, they are matched with the industrially available cathodes (NMC-111) to study the full cell performance in the T-cell setup. The assembled full cells are cycled in different voltage ranges with a current rate of 0.1C. The corresponding results are presented in Figure 7. A list of the potentials of the NMC cathode and the CuO anode that were measured with an auxiliary reference electrode is given in Table 1. When the full cell voltage increases from 0.7 to 4.0 V, the corresponding potential ranges of NMC and CuO are 3.68-4.35 V vs. Li/Li^+ and 2.98-0.29 V vs. Li/Li^+, respectively. These ranges are within the "typical" potential ranges of both the cathode and the anode.

The specific capacities of the full NMC/CuO cells, depicted in Figure 8a, vary according to the different adopted cut-off voltages. The occurring differences are related to the voltage regions of the anodes and cathodes. For example, the long voltage region (1.2-1.7 V) presented at the charge/discharge curve of 0.7-4.0 V is caused by the Li insertion/de-insertion into/from NMC at ~ 3.7 V. This region is absent for the curves measured within the other voltage ranges. Meanwhile, as regarding to the long-term cycling performance, all the three cells with the selected voltage ranges show high capacity retentions after 40 CC/CV cycles at 0.1C (Figure 9b). However, it is not surprising that the Coulombic efficiencies of the assembled full cells are quite low. This is due to irreversible reactions between CuO and Cu, as has already been discussed in the previous sections dealing with the Li metal cell setup. Besides, an obvious increase of the specific capacity is observed in the range of 0.7-4.0 V during the initial cycles, which cannot be found for other voltage ranges. This can be explained with reactions at the CuO anode. When the full cell voltage is changed from 1.3 to 0.7 V, the potential of the CuO

electrode increases from 2.48 to 2.98 V vs. Li/Li^+. This range, as has been previously discussed, is related to the transformation of Cu to Cu_2O and $Cu_{2-x}O$.

After a careful comparison of different potential ranges of the cathode and the anode, the NMC 111/CuO full cell with the voltage range of 0.7-4.0 V shows both high capacity and stable long-term cycling performance. The rate capability as well as the high-current cycling retention was investigated within this voltage range, as shown in Figure 10. The specific discharge capacities obtained at 0.1 to 10C are listed in Table 2. Even at the current rate of 10C, the capacity of 290 ± 7 mAh/g is still kept. When the current rate returns gradually to 0.1C, the discharge capacity of 635 ± 4 mAh/g is retained with a capacity retention of 96 %. This indicates that even at large current rates, the cell does not suffer irreversibly.

In order to understand the cycling performance at higher current rates, the NMC/CuO full cell is cycled under 1C for 100 CC/CV cycles. The charge/discharge curves are depicted in Figure b. After the formation process, a specific discharge capacity of 618 ± 2 mAh/g is reached at 1C. The capacity retention after 100 cycles is 85 %. During the first 70 cycles, the cell experiences almost no capacity decay, and the gradual decay can be prevented by the addition of an electrolyte additive. This study will be extended in our following reports. All over all, the full cell shows excellent electrochemical properties both at low and high current rates, with high capacity retentions that can be compared with the traditional graphite/NMC full cells.

To investigate the electrolyte composition of the aged CuO/NMC cells, the GC-MS and IC methods are combined to check the organic compounds as well as LiPF6 decomposition in the aged electrolytes. The chromatograms are shown in Figure 11. For non-volatile compounds, e.g., di-and monofluorophosphates, the separation by IC has been successfully carried out within our group.[26, 36, 37] For the cells investigated, the adopted electrolyte is 1 mol dm^{-3} $LiPF_6$ dissolved in 3:7 (wt%) EC: DMC mixture, which is a typical LIB electrolyte composition.[38,

[39] Based on $LiPF_6$ being highly hygroscopic, the electrolytes are always contaminated with a certain amount of water that can accelerate the decomposition of the conducting salt to LiF and PF_5. This subsequently results in hydrofluoric acid (HF) formation.[40, 41] These decomposition products have in the long-term a negative influence on the performance of the lithium-ion batteries.[40, 42] For volatile compounds, especially the common decomposition product of the low viscosity solvent dimethyl carbonate (dimethyl 2, 5-dioxahexane dicarboxylate, DMDOHC), which has been detected by many groups regarding its effect on lowering the ionic conductivity of the electrolyte and reduce the battery life[r1],[43-45] the existence is proved by GC-MS measurements. However, in both the IC and GC-MS chromatograms, no further electrolyte decomposition products are detected.

4. Discussion[r2]

In this paper, a nanostructured CuO electrode was prepared that possessed a very high capacity (in a Li metal setup), which cannot be explained by the theoretical capacity of Cu_2O (with copper having the oxidation state +1). Such capacity can only be explained by a higher oxidation state of Cu than +1. This oxidation state was confirmed by XAS.

The structure analysis using XRD and selected area electron diffraction revealed presence of Li_2O, Cu and Cu_2O, but not the presence of CuO, which would be needed to achieve a higher oxidation state of copper than +1.

Later, an explanation of the observed phenomena is given: It follows from the SQUID measurements that Cu^{2+} is present in the material under study because of the defect crystal structure of cubic $Cu_{2-x}O$ containing vacancies on the positions of copper atoms. This result is compatible both with the result of the structure studies by XRD and ED and with the results of XAS. Finally, the high measured capacity is explained by an “additional oxidation” of the copper ions in the defect-rich cubic $Cu_{2-x}O$, which is most probably located at the rims of cubic

Cu_2O nanocrystallites. The additional oxidation of Cu_2O rims could be responsible for the capacity increase as compared with defect-free Cu_2O. Thus, the crystallite size plays a crucial role in the charging and discharging process. Still, the monoclinic CuO was not observed in samples that experiences more cycles, because the energy of formation is probably too high for this phase. An illustrative scheme of the reaction mechanism for the nanostructured CuO electrodes has been presented in Figure 14.

4. Conclusions

Nanostructured CuO electrodes were prepared as high capacity anodes for lithium metal and lithium ion batteries with commercially available raw materials. A stable specific capacity of ≈580 mAh/g was achieved during 40 constant current cycles at 0.1C for the self-assembled CuO/Li metal cells. During cycling, an SEI was found to be formed after the 1st delithiation, while the enhanced Li^+ transport was confirmed to be the key factor in improving the electrochemical performance. The addition of a constant voltage step during the first 5 cycles at 0.1C can effectively promote the Li^+ diffusion in the electrode and enhance the capacity.

Moreover, as a main focus, a deep insight into the reaction mechanism between Li and CuO is gained by analyzing the initial lithiation/delithiation cycles, in which changes in the phase composition, morphology and volume of the phase mixture takes place.

With the help of XAS, SQUID, SEM and TEM, it is found that during the 1st lithiation, CuO is reduced to Cu. At 0.02V (in the lithiated state), only particles consisting of nano-crystalline Cu and Li_2O are detected. When the electrode is re-oxidized to 3 V, the transformation of Cu to a mixture of Cu, Cu_2O and $Cu_{2-x}O$ ($x < 1$) occurs. Nevertheless, during the following repeated delithiation processes, more and more Cu and Cu_2O is oxidized to $Cu_{2-x}O$ ($x < 1$), and the average oxidation state of the copper moves forward to +2, while small amounts of Cu and

Cu_2O are still kept in the delithiated electrodes. All these combined results reveal high and stable specific capacities and a high capacity retention for the CuO/Li metal cells.

When matched with a commercial NMC-111 cathode for the investigation of full cells, the corresponding CuO/NMC-111 full cell displays a specific capacity of 660 ± 2, 595 ± 4 and 290 ± 7 mAh/g at 0.1, 1 and 10 C within the voltage range of 0.7 – 4.0 V, revealing its high rate capability. Moreover, after 200 CC/CV cycles at 1C, the capacity retention of the cell is 85 %. According to the results of GC-MS and IC analyses, no further electrolyte decomposition products are found in the aged electrolytes, indicating a high stability of the electrolyte during long-term cycling. However, it should also be noted, that the energy efficiencies of the obtained NMC/CuO cell at 0.1 and at 1C are 68 and 52 %, respectively.

5. Experimental Section

Electrode preparation: Commercially available nano-sized CuO spherical particles (< 50 nm 98 %, Sigma Aldrich, Germany) were used as the starting materials. To obtain high capacity CuO electrodes, 80 wt% of the active material, 10 wt% of carboxymethyl cellulose (CMC, WALOCEL CRT 2000 PPA 12, Dow Wolff Cellulosics, Germany) and 10 wt% of the conducting carbon black agent (Super P C65, Imerys, France) were mixed (80 %, H_2O based slurry) and underwent high-speed ball milling (pulverisette 4 by FRITSCH, Germany (400 rpm, -800 rpm) with a 45 ml jar and 3 * 10 mm, 11* 5 mm diameter balls made of zirconium oxide) for 50 minutes to get a homogeneous slurry. The CMC-based binder was previously dissolved in deionized water to obtain a 3 wt% solution. The slurry was then cast on a clean copper foil by using a laboratory doctor blade with a wetting thickness of 260 µm. After drying at 60 ℃ for 2 hours, the foil was punched into disk electrodes with a diameter of 12 mm and further dried at 120 ℃ for 24 hours under vacuum. The obtained electrodes have an average mass loading of ~ 4 mg.

Electrochemical investigations: To investigate the electrochemical performance of the obtained electrodes, coin cells with Li metal (2032) and 2-electrode full cells in the T-cell setup were assembled in an argon-filled glovebox (mBraun, Germany) with less than 1 ppm of oxygen and water contents. For coin cell assembly, Celgard 2500 (polypropylene, Celgard, U.S.A) separator was adopted, and Li metal (Rockwood Lithium, battery-grade, Germany) was used as the counter electrode with the addition of 90 µL of the electrolyte. For full cells in the T-cell setup cell assembly, a six-layer Freudenberg 2190 (polyethylene fleece, Freudenberg, Germany) was used as the separator and a commercially available $LiNi_{1/3}Mn_{1/3}Co_{1/3}O_2$ (NMC-111) as the cathode. The cells were filled with 150 µL of the electrolyte. A 1 molar solution of lithium hexafluorophosphate ($LiPF_6$) in a 1:1 mixture (by weight) of ethylene carbonate (EC) and dimethyl carbonate (DMC) (BASF, Germany) was used as the standard electrolyte (quoted as LP30).

Electrochemical cycling was conducted with the assembled cells on a Maccor 4300 battery tester (Maccor, USA). The voltage range for Li metal cell investigation was 0.02 – 3 V and the voltage range for full cell investigation was 0.7 – 4.2 V, respectively. The C-rate varied from 0.1 – 10C. During the investigation of the potentials for cathodes and anodes for full cells, a 3-electrode setup was adopted, with an addition of the Li reference electrode, with two auxiliary cables added at the cathode and the reference electrode. The cells were cycled at 20 °C in an environmental test chamber (KB 400, Binder, Germany). The specific capacity calculation was based on the CuO electrode side. To guarantee the reproducibility of the electrochemical results, at least two cells per sample for each investigation procedure were prepared. The anode: cathode capacity balance is 1:1. The impedance measurement was carried out with Maccor frequency response analyzer (FRA) with the frequency from 30 kHz to 0.01 Hz and an excitation amplitude of 10 mV.

The mean discharge voltages of cathodes from cells with different electrolyte systems (Mean voltage calculated as energy divided by capacity) were extracted for every cycle at the end of the lithiation step.

Scanning electron microscopy: Scanning electron microscopy (SEM) was used to investigate electrode surfaces and morphology changes of the material. Numerous areas (at least ten) per sample were analyzed in an Auriga Crossbeam workstation (Carl Zeiss, Germany) with a field emission gun (Schottky-type). Samples were washed with dimethyl carbonate (DMC) and analyzed at an acceleration voltage of 3 kV.

X-ray powder diffraction: The investigation of the phase evolution and crystalline changes during the electrochemical cycling was conducted by the *in situ* X-ray powder diffraction measurements, which were performed on a D8 Advance diffractometer (Bruker, Germany) with Cu Kα radiation (λ=0.154 nm) equipped with a Lynxeye detector. A self-made *in situ* XRD electrochemical cell was assembled with a Beryllium (Be) window as the current collector.[46] The cell was operated in the voltage range of 0.02 – 3 V. The *in situ* cell was cycled at a current rate of C/20 and the corresponding *in situ* XRD patterns were recorded every three hours. A constant voltage step is added after every lithiation for the specific recording at the voltage of 0.02 V. The phase analysis of the fresh electrode was performed by Rietveld refinement of X-ray diffraction pattern. For the quantitative analysis of the diffraction pattern the software package MAUD was used.[Lut1]

Transmission electron microscopy: The local microstructure and SEI thickness were investigated by use of an aberration corrected analytical high resolution microscope JEM 2200 FS (JEOL, Japan) at an accelerating voltage of 200 kV. The structure and composition of the existing phases were determined by selected area electron diffraction (SAED) and energy dispersive X-ray spectroscopy (EDS). For the background fit of the integrated SAED pattern a

power law model was applied. For the TEM and SAED investigations, the active material was carefully removed from the current collector and dispersed by ultrasonic treatment in DMC for exact three minutes for each sample. A drop of the dispersion was placed on a Ag support grid covered with a carbon hole film and dried. All these preparations steps were done in a glove box under protecting Ar atmosphere. During the transport and the sample mounting into the TEM, the samples were protected by an Ar filled AtmosBag.

X-ray absorption spectroscopy: The Cu K-edge X-ray absorption spectra were recorded in the transmission mode at beamline KMC-2 of the BESSY-II synchrotron light source, Berlin, Germany. A graded Si–Ge (111) double crystal monochromator was used in this beamline and higher harmonics were rejected by detuning the monochromator such that the intensity of the beam on the sample was 65% of the maximum possible intensity. A gas-filled ionization chamber (70% nitrogen, 30% argon) was used so as to get a good signal to noise ratio. Pure copper foil (~ 10 µm thick) was measured simultaneously with each sample for absolute energy calibration of the monochromator. The data were pre-processed as prescribed elsewhere using the software ATHENA of the package IFEFFIT.[47-48] All spectra were energy-calibrated with respect to the first peak in the pure Cu derivative spectrum.

Magnetization Measurement using the Superconducting Quantum Interference Device: Magnetization measurements of the electrochemically reduced and subsequently oxidized copper oxide (m = 18.64 mg) were performed between 2 and 300 K in external magnetic fields up to 6 T (Fig. 1), and between -5 and 5 T at 10 K and 300 K, using a SQUID magnetometer (MPMS) from Quantum Design. First, the diamagnetic response of the gelatin capsule used as a sample holder was checked and then subtracted from magnetization values in further measurements. The diamagnetic susceptibility for a typical capsule used in the experiment was measured as $\chi_{capsule} \sim -4.0 \times 10^{-7}$ emu/g*Oe at 10 K. This value is almost temperature-

independent within 5% from 2 to 300 K and corresponds to about 1% of the sample susceptibility.

Electrolyte extraction after cycling (= electrochemical aging): The electrolyte was extracted in the same way for coin cells and T-full cells. After electrochemical cycling, cells were opened in a glovebox (H_2O < 1 ppm, O_2 < 1 ppm, mBraun, Germany) to protect them against moisture and oxygen. The separator was taken out of the cell immediately and put into a 1.5 mL Eppendorf Safe-Lock Tube (Eppendorf, Germany) in order to prevent electrolyte evaporation. The Safe-Lock Tube was prepared with an insertion of a pipette tip which acted as the distance piece between the bottom of the Safe-Lock Tube and the separator. The Safe-Lock Tube with the separator was centrifuged for 15 minutes at 8500 rounds per minute with a Galaxy SD Microcentrifuge (VWR International GmbH, Germany). With this method, the pure electrolyte could be extracted out of the separator. For GC-MS and IC measurements, 10 µL of the electrolyte was diluted 1/100 (v/v) with acetonitrile (99.9 %, LC-MS grade, VWR International, Germany).

GC-MS: The GC-MS experiments were conducted on a Shimadzu GCMS-QP2010 Ultra instrument with an AOC-5000 Plus as auto sampler, an OPTIC-4 injection system (all Shimadzu, Germany) and a Supelco SLB-5ms column (30 m × 0.25 mm × 0.25 µm, Sigma-Aldrich, Germany). The setup control and data analysis was performed by the software of GCMS Real Time Analysis and GCMS Postrun Analysis (Shimadzu, Germany). 1 µL of the diluted sample was injected at 230 °C. The system runs with helium (purity of 6.0, Westfalen Gas, Germany) as the carrier gas with a column flow of 1 mL/min and a split ratio of 1:50. The column oven program was set to the starting temperature of 40 °C for 1 min. Then, the temperature was increased with a speed of 25 °C/min to 230 °C and with a holding time of 3.4 min. Samples were measured in the electron ionization (EI) mode at an ion source

temperature of 200 °C. The filament voltage was set to 70 V and the detector voltage was set relative to tuning in a range of m / z = 30 - 350.

IC: To detect the ionic decomposition products, an IC equipped with a conductivity detector was used in this study. The column adopted was Metrosep A Supp 7 with the matching guard column Metrosep A 4/5 guard (Metrohm, Switzerland). The column had the following dimensions: 250 mm length x 4.0 mm interior diameter and 5 µm particle size. The IC consisted of a suppressor applying a 100 mmol/L sulfuric acid solution (H_2SO_4, 99.9 %, Merck KGaA, Germany) purchased from Sigma-Aldrich Chemie GmbH (Germany) for chemical suppression. The system was controlled by MagIC NetTM 3.1 (Metrohm, Switzerland). The mobile phase consisted of 4.2 mmol/L sodium carbonate (Na_2CO_3, 99.9 %) and 2.0 mmol/L sodium bicarbonate ($NaHCO_3$, 99.7 %), both purchased from Merck KGaA (Germany). The carbonate salts were dissolved in a mixture of 30 vol% acetonitrile (99.9 %, LC-MS grade, VWR International, Germany) and 65 vol. % Milli-Q water, obtained by a Millipore Milli-Q system (USA). The flow rate of the mobile phase was 0.6 mL/min. Sample injection was provided by an autosampler and a 6-way injection valve with a sample loop of 10 µL.

Supporting Information

Supporting Information is available from the Wiley Online Library or from the author.

Acknowledgements

The authors would like to thank the German Research Foundation (DFG) for funding this work within the joint Priority Program 1473 “Materials with New Design for Improved Lithium Ion Batteries – WeNDeLIB”. The allocation of beamtime at KMC-2, BESSY II, is gratefully acknowledged.

Received: ((will be filled in by the editorial staff))
Revised: ((will be filled in by the editorial staff))
Published online: ((will be filled in by the editorial staff))

References

[1] H. Ikeda, S. Narukawa, *J. Power Sources*, **1983**, *9*, 329.

[2] Y. Matsuda, K. Teraji, Y. Takasu, *Denki Kagaku.* **1976**, *44*, 363.

[3] R. Bates, Y. Jumel, J. P. Gabano, *Lithium Batteries,* Academic Press, New York: **1983**.

[4] P. Novak, *Electrochim. Acta*, **1985**, *30*, 1687.

[5] T. Ohzuku, Z. Takehara, S. Yoshizawa, *Denki Kagaku,* **1978**, *46*, 407.

[6] T. Ohzuku, Z. Takehara, S. Yoshizawa, *Electrochim. Acta*, **1979**, *24*, 219.

[7] J. Y. Xiang, J. P. Tu, J. Zhang, J. Zhong, D. Zhang, J. P. Cheng, *Electrochem. Commun.*, **2010**, *12*, 1103.

[8] P. Poizot, S. Laruelle, S. Grugeon, L. Dupont, J. M. Tarascon, *Nature*, **2000**, *407*, 496.

[9] H. Buqa, R. I. R. Blyth, P. Golob, B. Evers, I. Schneider, M. S. Alvarez, F. Hofer, F. P. Netzer, M. G. Ramsey, M. Winter, *Ionics,* **2000**, *6*, 172.

[10] M. Winter, J. O. Besenhard, *Handbook of Battery Materials,* Weinheim: VCH, **1999**, Vol. 3.

[11] J. O. Besenhard, M. Winter, *ChemPhysChem*, **2002**, *3*, 155.

[12] H. Jia, R. Kloepsch, X. He, M. Evertz, S. Nowak, J. Li, M. Winter, T. Placke, *Acta Chimica Slovenica*, **2016**, *63*, 470.[RA3]

[13] S. Q. Wang, J. Y. Zhang, C. H. Chen, *Scr. Mater.*, **2007**, *57*, 337.

[14] C. Li, W. Wei, S. Fang, H. Wang, Y. Zhang, Y. Gui, R. Chen, *J. Power Sources*, **2010**, *195*, 2939.

[15] J. Cabana, L. Moncunduit, D. Larcher, M. R. Palacin, *Adv. Energy Mater.*, **2010**, *22*, E170.

[16] V. R. Palkar, P. Ayyub, S. Chattopadhyay, M. Multani. *Phys. Rev. B*, **1996**, *53*, 2167.

[17] M. Winter, J. O. Besenhard, J. H. Albering, J. Yang, M. Wachtler, *Prog. Batteries Battery Mater.*, **1998**, *17*, 208.

[18] X. P. Gao, J. L. Bao, G. L. Pan, H. Y. Zhu, P. X. Huang, F. Wu, D. Y. Song, *J. Phys. Chem. B*, **2004**, *108*, 5547.

[19] P. Poizot, C.-J. Hung, M. P. Nikiforov, E. W. Bohannan, J. A. Switzer, *Electrochem. .Solid-State Lett.*, **2003**, *6*, C21.

[20] J. C. Park, J. Kim, H. Kwon, H. Song, *Adv. Mat.*, **2009**, *21*, 803.

[21] H. Schranzhofer, J. Bugajski, H. J. Santner, C. Korepp, K.-C. Möller, J. O. Besenhard, M. Winter, W. Sitte, *J. Power Sources*, **2006**, *153*, 391.

[22] M. Winter, *Zeitschrift für Physikalische Chemie International Journal of Research in Physical Chemistry and Chemical Physics*, **2009**, *223*, 1395.

[23] S. Grugeon, S. Laruelle, R. Herrera-Urbina, L. Dupont, P. Poizot, J. M. Tarascon, *J. Electrochem. Soc.*, **2001**, *148*, A285.

[24] L. Hu, Y. Huang, F. Zhang, Q. Chen, *Nanoscale*, **2013**, *5*, 4186.

[25] R. Wu, X. Qian, F. Yu, H. Liu, K. Zhou, J. Wei, Y. Huang, *J. Mater. Chem. A*, **2013**, *1*, 11126.

[26] S. Ko, J. I. Lee, H. S. Yang, S. Park, U. Jeong, *Adv. Mat.*, **2012**, *24*, 4451.

[27] Y. Hu, X. Huang, K. Wang, J. Liu, J. Jiang, R. Ding, X. Ji, X. Li, *J. Solid State Chem.*, **2010**, *183*, 662.

[28] Q.-C. Zhuang, T. Wei, L.-L. Du, Y.-L. Cui, L. Fang, S.-G. Sun, *J. Phys. Chem. C*, **2010**, *114*, 8614.

[29] J. Kasnatscheew, M. Evertz, B. Streipert, R. Wagner, R. Klöpsch, B. Vortmann, H. Hahn, S. Nowak, M. Amereller, A.-C. Gentschev, P. Lamp, M. Winter, *Phys. Chem. Chem. Phys.*, **2016**, *18*, 3596.

[30] A. Débart, L. Dupont, P. Poizot, J. Leriche, J. Tarascon, *J. Electrochem. Soc.*, **2001**, *148*, A1266.

[31] H. Wieder, A. W. Czanderna, *J. Phys. Chem.*, **1962**, *66*, 816.

[32] E.G. Clarke, A.W. Czanderna, *Surf. Sci.*, **1975**, *49*, 529.

[33] J. Wong, F. W. Lytle, R. P. Messmer, D. H. Maylotte, *Phys. Rev. B*, **1984**, *30*, 5596.

[34] C. Chen, L. He, L. Lai, H. Zhang, J. Lu, L. Guo, Y. Li, *J. Phys.: Condens. Matter*, **2009**, *21*, 145601.

[35] A. Punnoose, H. Magnone, M. S. Seehra, J. Bonevich, *Phys. Rev. B*, **2001**, *64*, 174420.

[36] L. Terborg, S. Weber, F. Blaske, S. Passerini, M. Winter, U. Karst, S. Nowak, *J. Power Sources*, **2013**, *242*, 832.

[37] L. Terborg, S. Nowak, S. Passerini, M. Winter, U. Karst, P. R. Haddad, P. N. Nesterenko, *Anal. Chim. Acta*, **2012**, *714*, 121.

[38] K. Tasaki, A. Goldberg, M. Winter, *Electrochim. Acta*, **2011**, *56*, 10424.

[39] R. W. Schmitz, P. Murmann, R. Schmitz, R. Müller, L. Krämer, J. Kasnatscheew, P. Isken, P. Niehoff, S. Nowak, G.-V. Röschenthaler, *Prog. Solid State Chem.*, **2014**, *42*, 65.

[40] S. F. Lux, J. Chevalier, I. T. Lucas, R. Kostecki, *ECS Electrochem. Lett.*, **2013**, *2*, A121.

[41] S. Zugmann, D. Moosbauer, M. Amereller, C. Schreiner, F. Wudy, R. Schmitz, R. Schmitz, P. Isken, C. Dippel, R. Müller, *J. Power Sources*, **2011**, *196*, 1417.

[42] S. S. Zhang, *J. Power Sources*, **2006**, *162*, 1379.

[43] S. Takeshi, T. Abe, Y. Iriyama, M. Inaba, Z. Ogumi, *J. Electrochem. Soc.*, **2005**, *152*, A2046.

[44] E. S. Takeuchi, H. Gan, M. Palazzo, R. A. Leising, S. M. Davis, *J. Electrochem. Soc.*, **1997**, *144*, 1944.

[45] S. Takeshi, T. Abe, Y. Iriyama, M. Inaba, Z. Ogumi, *J. Power Sources*, **2005**, *150*, 208.

[46] D. Bresser, E. Paillard, R. Kloepsch, S. Krueger, M. Fiedler, R. Schmitz, D. Baither, M. Winter, S. Passerini, *Adv. Energy Mater.*, **2013**, *3*, 513.

[47] S. D. Kelly, K. M. Kemner, J. B. Fein, D. A. Fowle, M. I. Boyanov, B. A. Bunker, N. Yee, *Geochim. et Cosmochim. Acta*, **2002**, *66*, 3855.

[48] B. Ravel, M. Newville, *J. Synchrotron Radiat.*, **2005**, *12*, 537.

[Rie1] H.M. Rietveld, *Acta Cryst.*,**1967**, *22*, 151.

[Rie2] H.M. Rietveld, J. *Appl. Cryst.*,**1969**, *2*, 65.

[Lut1] L. Lutterotti, S. Matthies, H.-R. Wenk, *IUCr: Newsletter of the CPD*, **1999**, *21*, 14.

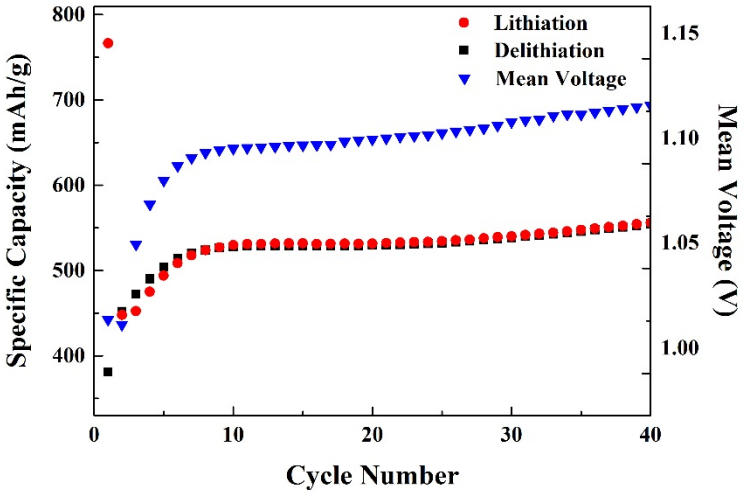

Figure 1. Cycling performance of nano CuO/Li metal cells for 40 CC cycles at 0.1C. The increasing mean voltages of the corresponding cycles indicates a decrease of the internal resistance.

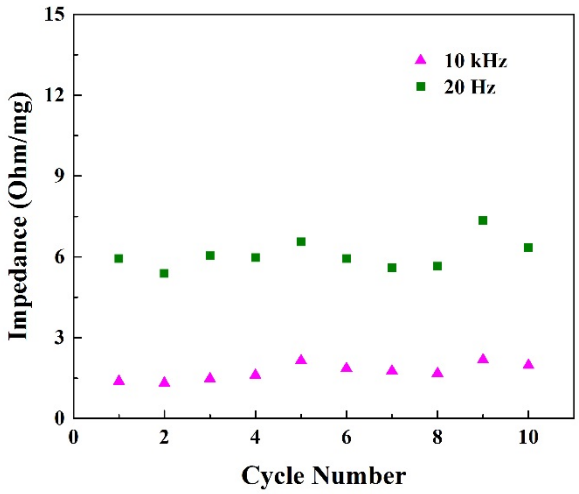

Figure 2. Electrochemical impedance spectroscopy results of the nano CuO/Li cells at the frequencies of 20 and 10,000 Hz taken during 10 CC cycles at 0.1C shows a constant charge transfer resistance (20 Hz) and constant contact resistance (10 kHz).

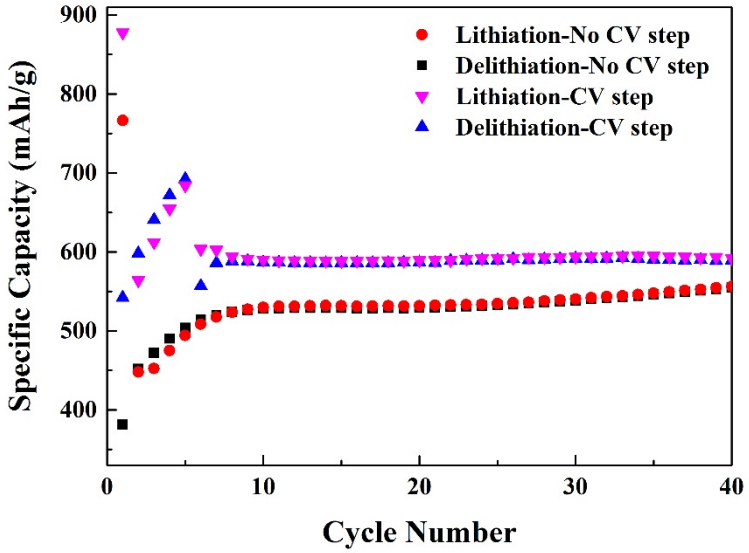

Figure 3. Cycling performance of the nano CuO electrodes after 40 CC cycles at 0.1C with and without a constant voltage step during the formation process.

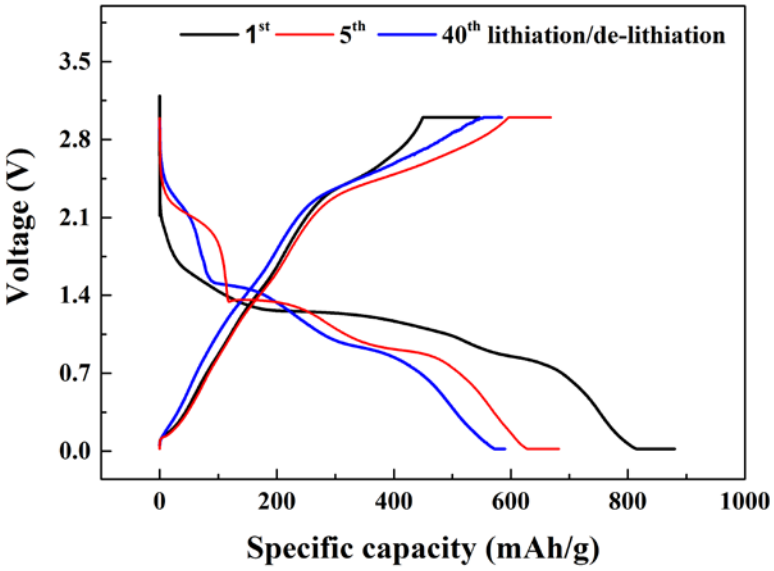

Figure 4.1st, 5th and 40th voltage profiles (CC/CV cycling) of the nano CuO/Li cells at the rate of 0.1C.

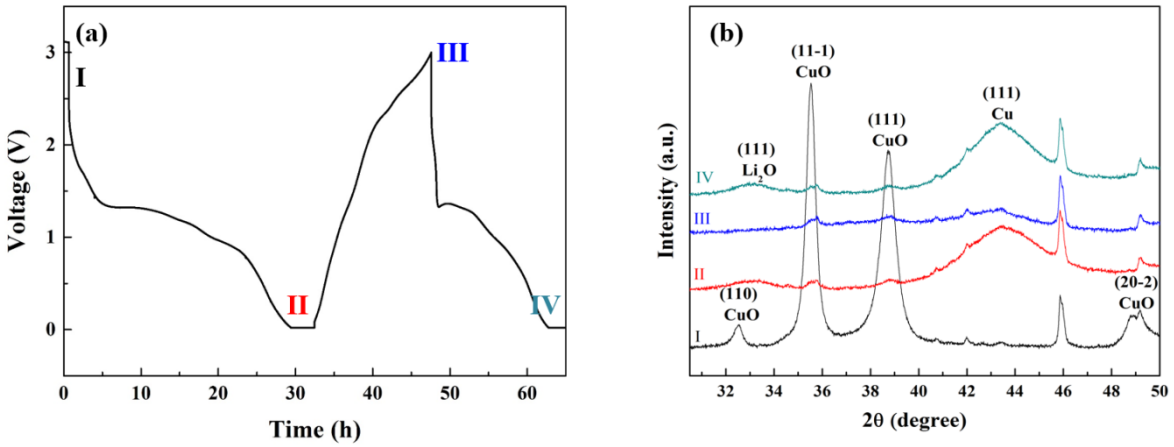

Figure 5. (a) Lithiation/delithiation curves for CuO in the *in situ* XRD cell during cycling, (b) *in situ* XRD [RA4]patterns collected at indicated states of lithiation/delithiation. The unlabeled reflections correspond to the characteristic reflections of the Be current collector and its impurities.

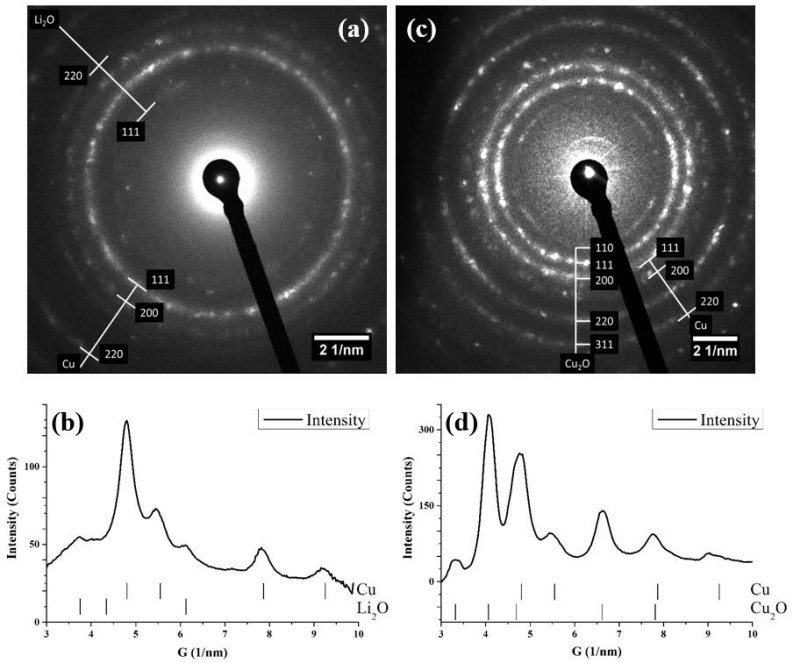

Figure 6. SAED patterns and integrated intensity distributions of the nano CuO electrode after the initial lithiation (a) and (b), as well as after the initial delithiation process (c) and (d) shows the phase composition of Cu and Li_2O for the lithiated state and the presence of Cu and Cu_2O

in the de-lithiated state. The scattering vector $\vec{G}$ is connected to the real space lattice spacing d by $d = \frac{1}{|\vec{G}|}$.

Figure 7. Normalized Cu K-edge XAS spectra of the nano CuO electrode at different stages of lithiation. In the figure, 0.02V(1st L) stands for 1st lithiation at the voltage of 0.02 V, 2.25V(1st D) stands for 1st lithiation at the voltage of 2.25 V, 3.0V(1st, 5th, 10thD) stand for 1st , 5th, 10th delithiation at the voltage of 3.0 V.

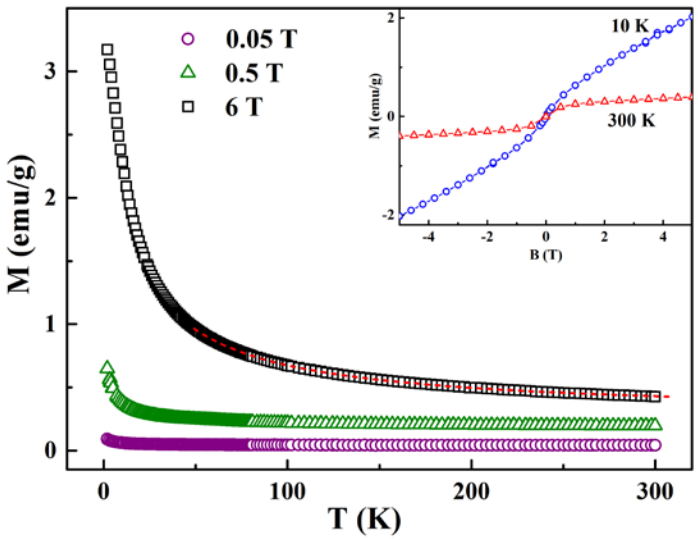

Figure 8. Temperature dependence of magnetization of $Cu_{2-x}O$ at different field strengths. Inset: Field dependence of magnetization at 10 K and 300 K. Red dashed line: Curie-Weiss fit (see text).

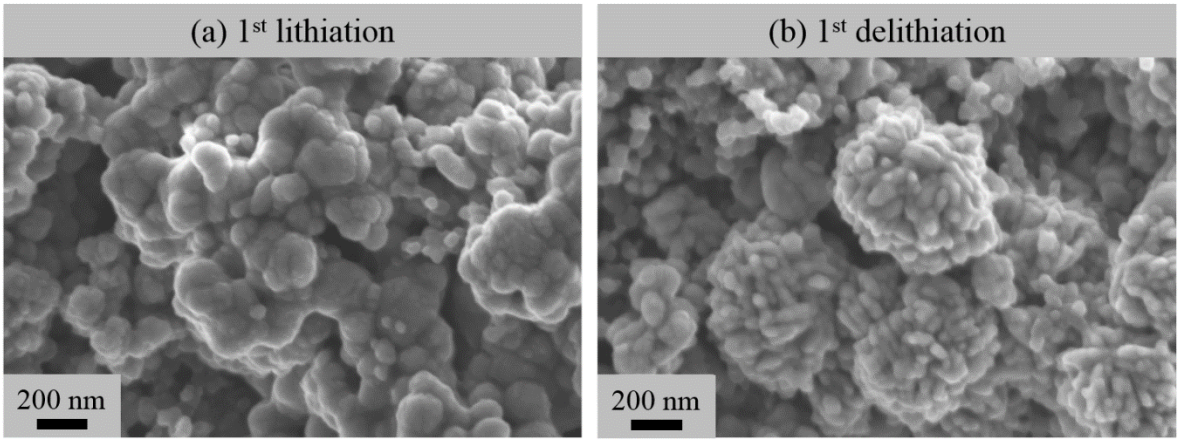

Figure 9. SEM images of the nano CuO electrode (a) after 1st lithiation, (b) after 1st delithiation.

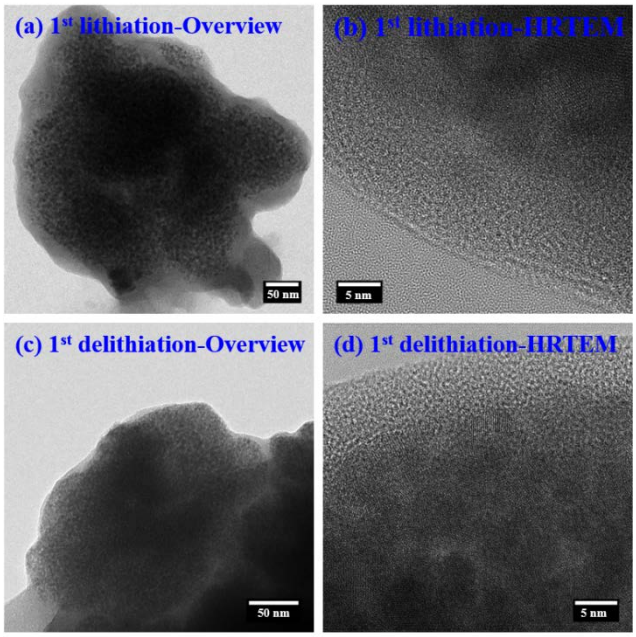

Figure 10. TEM micrographs of the nano CuO electrode (a) and (c) overviews, (b) and (d) HRTEM micrographs after the initial lithiation (top)/delithiation (bottom) shows a smaller thickness of the amorphous SEI layer surrounding the particles. The crystallite size is below 5 nm for both states.

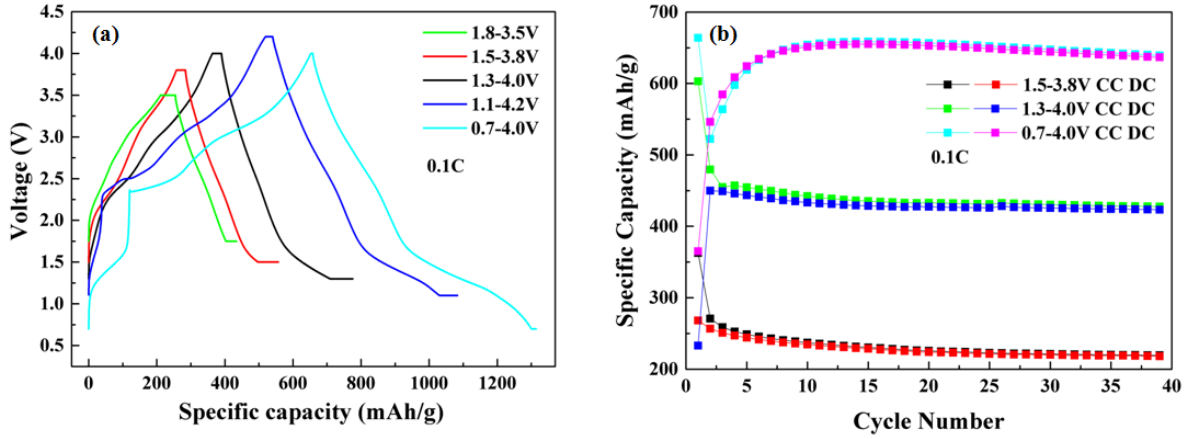

Figure 11. (a) Charge and discharge profiles and (b) the long term cycling performance of the assembled T-full cells with self-made CuO electrode as the anode and commercial NMC cathode within different voltage ranges. For (a), the specific capacity was selected after the formation step (0.1C for 5 CC cycles).

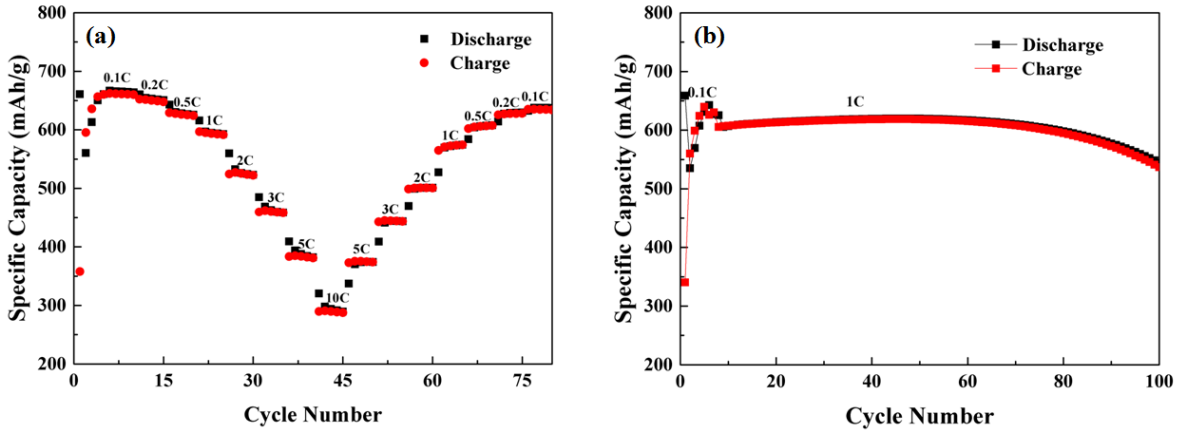

Figure 12. (a) Rate capability and (b) the 1C cycling performance of the assembled T-full cells with self-made CuO electrode as the anode and commercial NMC as the cathode within the voltage range of 0.7-4.0 V. A formation process of 0.1C for 5 CC/CV cycles was added for both investigation procedures.

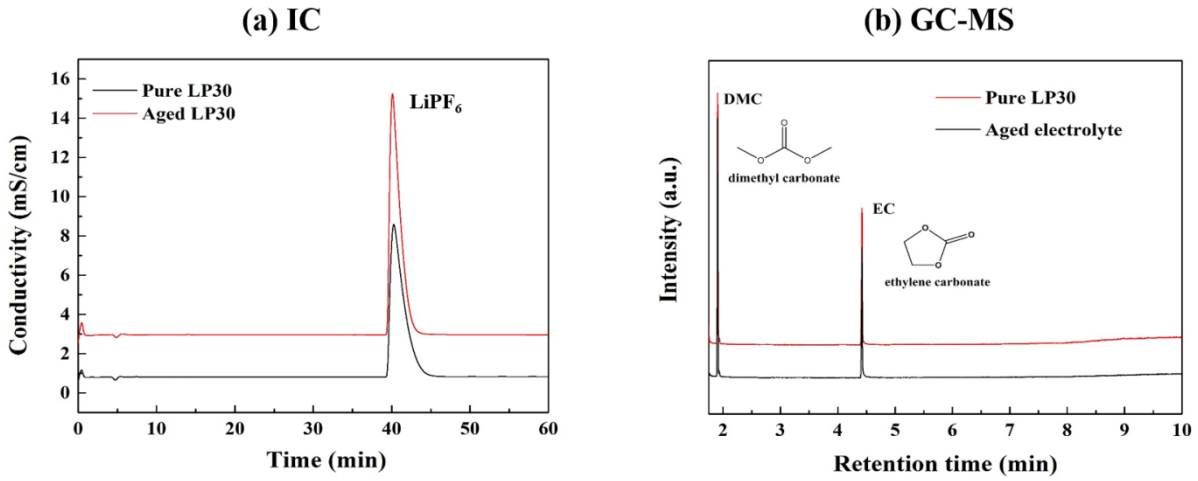

Figure 13. (a) IC and (b) GC-MS chromatograms of the pure and aged LP30 electrolyte. The aged electrolyte was extracted from the CuO/NMC cells which underwent 100 CC/CV cycles at 1C.

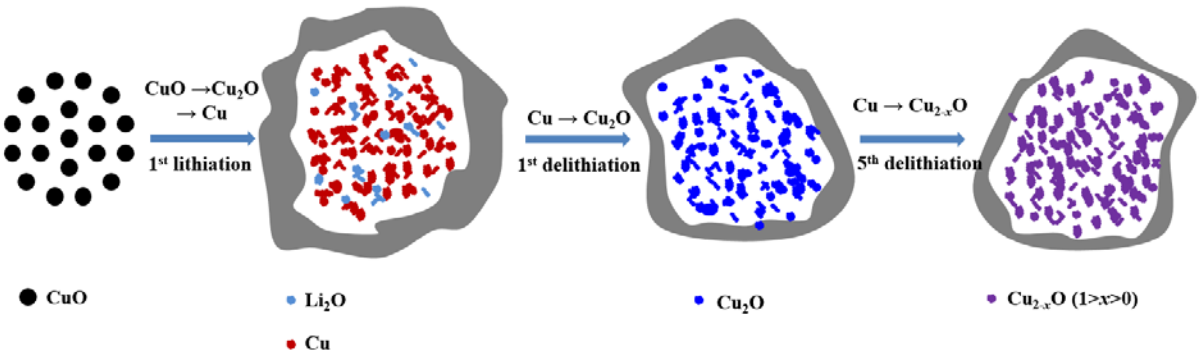

Figure 14. Proposed reaction mechanism for the nanostructured CuO electrodes during the intial lithiation/delithiation cycles, each color represents a different material, and the covering layer at the material surface represents the SEI. During the formations steps (CV) between the 1th and 5th cycle the oxidations state of Cu shifts towards +2, expressed by $Cu_{2-x}O$.

Table 1. List of the individual potentials of the NMC cathode and the CuO anode with the increase of the full cell voltage measured by a T-cell setup.

Voltage Full (V)	Potential Aux NMC (V)	Potential CuO (V)
0.70	3.68	2.98
0.90	3.71	2.81
1.10	3.77	2.66
1.30	3.78	2.48
1.50	3.79	2.29
1.75	3.80	2.05
3.50	4.24	0.74
3.60	4.28	0.68
3.80	4.31	0.51
4.00	4.35	0.35

Table 2. List of the specific capacities of CuO/NMC-111 full cells at different current rates.

C rate	0.1C	0.2C	0.5C	1C	2C	3C	5C	10C
Specific capacity* (mAh/g)	660 ± 2	651 ± 3	600 ± 4	595 ± 4	525 ± 3	460 ± 5	380 ± 8	290 ± 7

* The specific capacity of the full cell is calculated based on the CuO anode.

Supporting Information

Title: Investigation of Nano-Sized Cu(II)O As a High Capacity Conversion Material for Li Metal Cells and Lithium Ion Full Cells

*Yunxian Qian, Philip Niehoff, Dong Zhou, Robert Adam, Daria Mikhailova, Marcelina Pyschik, Markus Börner, Richard Klöpsch, David Rafaja, Gerhard Schumacher, Martin Winter, Helmut Ehrenberg, and Falko Schappacher**

Supplementary 1:

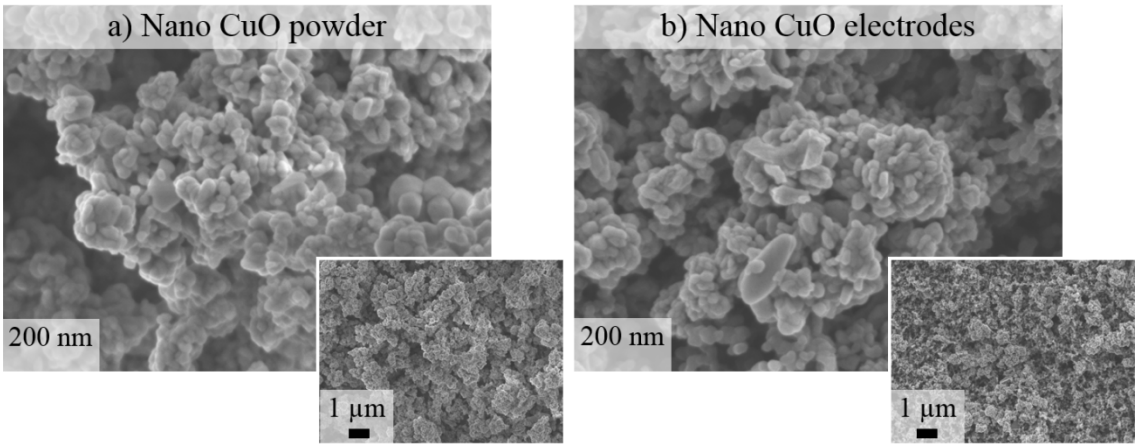

Figure S1: (a) and (b) SEM images of the pristine nano CuO particles and the resulting electrodes before cycling. The inlets are taken at a magnification of 5,000 times while the other images are taken at a magnification of 10,000 times.

Supplementary 2:

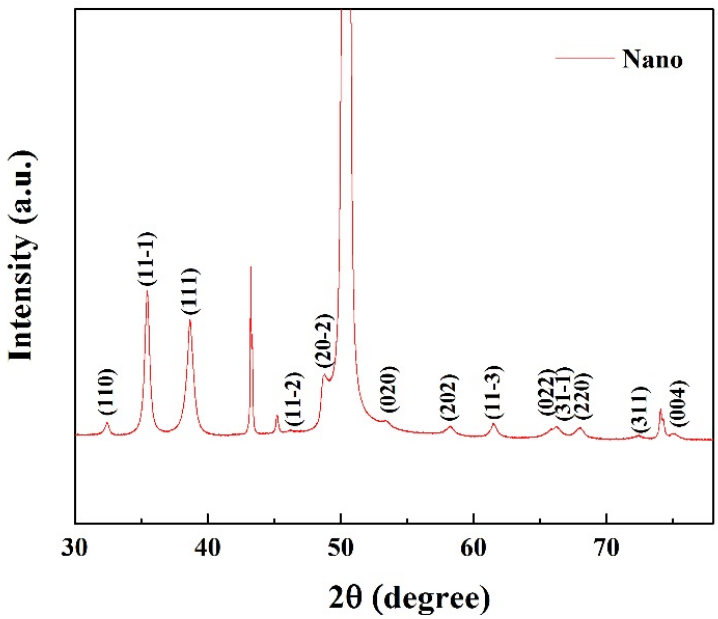

Figure S2: XRD pattern of the cast nano-crystalline CuO electrode[RA5]. The labeled reflections correspond to monoclinicCuO, while the unlabeled reflections correspond to the copper current collector.